All-atom molecular dynamics simulation of the [Fe(pyrazine)][Ni(CN)$_4$] spin-crossover complex. II. Spatiotemporal study of a bimorph actuator

Shiteng Mi, Gábor Molnár ⬤, Karl Ridier ⬤, William Nicolazzi ⬤,[*] and Azzedine Bousseksou[†]

LCC, CNRS & Université de Toulouse, 205 route de Narbonne, 31077 Toulouse, France

We present an atomistic approach, based on a realistic structure of the compound [Fe(pyrazine)][Ni(CN)$_4$], which provides a spatiotemporal description of the spin-crossover (SCO) phenomenon. The vibronic coupling is described through an intramolecular double-well potential, whereas the elastic interactions between the Fe centers are considered by an additional spin-state-dependent potential. The model is then investigated through molecular dynamics (MD) simulations. This work is separated into two papers. Part I [S. Mi *et al.*, Phys. Rev. B **109**, 054103 (2024)] reports on the methodology used to simulate the spin transition in the bulk material. The present Part II addresses the spatiotemporal dynamics (nucleation and growth) of the spin transition in a bimorph actuator, mimicking the operation of a nanoelectromechanical device. The spin-state configuration and local strain are calculated to explore both the spatiotemporal aspects of the spin-state switching and the resulting deformation of the bimorph cantilever, as a function of the cooperativity of the SCO material and the thickness of the films. We show that the spatiotemporal dynamics deviates from a single nucleation process since additional domains can be formed due to the lattice bending, whereas the associated elastic stresses lead to longer switching times and to incomplete transitions. A comparison with classical continuum mechanical theory reveals that the latter may be no more valid in the case of systems with ultrathin films. Interestingly, due to competing effects between the spin-state switching dynamics and the natural frequencies of the cantilever, damped oscillations are observed in the spin-state fraction and in the deformation of the cantilever before reaching a stationary state.

I. INTRODUCTION

During the past few years, the development of actuator devices, referring to devices that convert an input source of energy into controlled mechanical motion, has aroused extensive research interest in the fields of artificial muscles, medical technologies, and robotic industry [1–3]. Within this broad field, simple bimorph structures are among the most often employed systems. These devices, which consist of the superposition of two strips of a stimuli-responsive and an inactive material joined together throughout their length, are forced to bend under external stimulation due to the different strain arising in the two materials. The most common approach uses the thermal expansion mismatch of materials under heating and cooling. However, the potential applications of these conventional bimetallic actuators are strongly limited by the fact that the volume change induced by thermal expansion is generally too small and requires thus large temperature differences to produce large curvatures. To enhance the amplitude of bending, bimorph actuators were thus fabricated, incorporating materials exhibiting thermally induced phase transitions, such as the martensitic transition in shape memory alloys [4,5] or the insulator-to-metal transition in vanadium dioxide [6–8].

In this context, spin-crossover (SCO) complexes of transition metal ions (mostly Fe^{2+}), which exhibit a reversible solid-state phase transformation between their high-spin (HS) and low-spin (LS) electronic configurations, have recently attracted considerable attention. SCO materials usually show drastic modifications of their physicochemical properties [9–12]. Notably, for Fe^{II} SCO complexes, the metal-ligand bond lengths are known to increase by ∼10% (i.e., ∼0.2 Å) when switching from the LS to the HS state [13–15], which can give rise to an abrupt expansion of up to 22% of the unit-cell volume [16], indicating the fascinating potential of SCO materials for their possible integration into bimorph actuators [17]. This concept has been demonstrated by Shepherd *et al.* [18], followed by a series of works on various SCO-based bimorph structures, including thin films and composites, allowing for the construction of both macroscopic [19–25] and micro/nanoscale [17,26–30] bending actuators, displaying attractive actuating performance.

From a theoretical point of view, these various bimorph SCO actuators have been modeled using conventional continuum mechanical approaches, such as the Euler-Bernouilli beam theory or finite element simulations, which provide efficient means for device design. However, these approaches obviously ignore local, microscopic effects, particularly the spatiotemporal aspects of the spin transition, which become increasingly important in micro/nanoscale actuators. In addition, they rely on a comprehensive preliminary experimental characterization, having no ability of predicting material properties. To remove these bottlenecks, atomistic simulations

*William.nicolazzi@lcc-toulouse.fr
†Azzedine.Bousseksou@lcc-toulouse.fr

appear as an attractive alternative. Up to now, such simulations employed mostly spring-ball models, investigated either by Monte Carlo (MC) and/or molecular dynamics (MD) methods. Notably, such approaches allowed for reproducing the bending motion of biphasic SCO single crystals, mechanical interactions between substrates, and SCO films as well as elastic couplings in bimorph, core-shell SCO particles [31–44].

To overcome some limitations of previously employed atomistic modeling methods, such as the neglect of structural details and/or some *ad hoc* assumptions, regarding the time scale of the simulated events, in this paper, we employ all-atom MD simulations, relying on the realistic structure of an SCO compound. We employ an original force field (FF) able to simulate the SCO behavior, including the couplings between the electronic and structural degrees of freedom. This FF has been described in Part I of this work [45], devoted to the simulation of the thermally induced spin transition of the bulk $[Fe(pyrazine)][Ni(CN)_4]$ SCO compound. This FF is based on the consideration of the realistic, all-atom structure of the SCO material and the different interactions within and between SCO units. More specifically, the intramolecular vibronic coupling is modeled through the consideration of Fe–N interactions described by a double-well potential. The buildup of elastic stress induced by the spin-state switching has been considered by a two-body potential connecting the Fe centers and involving an elastic energy barrier. The height of this elastic energy barrier drives the cooperativity within the SCO structure, which has a direct effect on the nature of the spin transition. Using this FF, MD simulations have been carried out in the isothermal-isobaric ensemble using periodic boundary conditions to simulate the thermally induced spin-state switching in the bulk $[Fe(pyrazine)][Ni(CN)_4]$ material. We found that the model adequately reproduces the main experimental observations, including the switching temperatures, the thermal hysteresis loop, and changes of various structural parameters [45].

In the present Part II of this work, we use this all-atom MD method to investigate the spatiotemporal dynamics of the spin-state switching in a bimorph, nanoscale actuator made of the $[Fe(pyrazine)][Ni(CN)_4]$ complex and the associated actuating performance of the device. To form a bimorph structure, a few $[Fe(pyrazine)][Ni(CN)_4]$ layers have been simply set SCO inactive. The spin-state configuration and the local strain are calculated in real time together with the deflection of the bimorph cantilever as a function of the thickness of the inactive and active part of the structure. By modulating the strength of the intermolecular interactions, we have also investigated the influence of the cooperativity of the SCO material on the switching dynamics and actuation phenomena.

II. MODELS AND METHODS

The present MD simulations are performed using the large-scale atomic/molecular massively parallel simulator software package (LAMMPS) [46] using the FF described in Ref. [45]. As shown in Fig. 1, the studied structure consists of a parallelepiped cantilever composed of $4 \times 55 \times N_{tot}$ ($6 \leqslant N_{tot} \leqslant 12$) unit cells (along the x, y, and z directions, respectively) of the $[Fe(pyrazine)][Ni(CN)_4]$ SCO complex, corresponding to systems with ~22 800–44 280 atoms. The
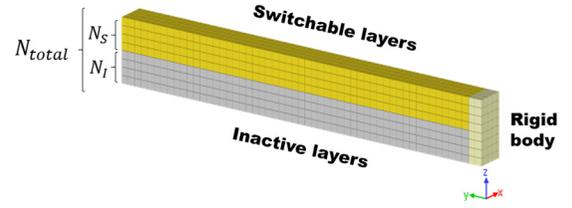

FIG. 1. Schematic view of the studied bimorph cantilever system, composed of $4 \times 55 \times N_{tot}$ unit cells (along the x, y, and z directions, respectively) of the $[Fe(pyrazine)][Ni(CN)_4]$ SCO material.

whole structure is initially prepared in the HS state. One extremity of the cantilever system was considered clamped. To do that, two unit cells along the y direction are set as a rigid body, meaning that the displacement of each atom is blocked. Along the z direction (i.e., the thickness of the cantilever), N_I $[Fe(pyrazine)][Ni(CN)_4]$ layers are set as inactive, which means that the Fe^{II} ions are fixed into the HS state by replacing the Fe–N double-well potential by a simple harmonic potential. Finally, the remaining $N_S(= N_{tot} - N_I)$ $[Fe(pyrazine)][Ni(CN)_4]$ layers constitute the active (switchable) part of the system, in which the Fe sites can switch between the HS and LS states. For each simulation, the structure is relaxed at 100 K, the temperature and pressure conditions being controlled by the Nosé-Hoover method [47,48]. All calculations were performed under the canonical (NVT) ensemble, and a timestep of 1 fs was used. The Voronoi analysis is conducted through the Voro++ software package [49] to calculate the atomic volume of Fe ions to identify the local spin state for each complex [45]. The atomic positions and strain mapping resulting from the simulation are visualized by means of OVITO software [50]. During the relaxation process, significant structural deformations appear due to the large difference of volume between the LS and HS states. To follow this structural relaxation, the local strain at each Fe atom is derived by considering the relative motion of its neighbors [51–53]. In detail, the relative position of two neighboring sites, denoted j and k, before strain, is given by

$$\Delta \boldsymbol{X}_{jk} = \boldsymbol{X}_k - \boldsymbol{X}_j, \tag{1}$$

where $\boldsymbol{X}_k$ and $\boldsymbol{X}_j$ are the position vectors of the atomic sites k and j, respectively, before strain. Accordingly, the relative position of these two atomic sites after strain is given by

$$\Delta \boldsymbol{x}_{jk} = \boldsymbol{x}_k - \boldsymbol{x}_j, \tag{2}$$

where $\boldsymbol{x}_k$ and $\boldsymbol{x}_j$ are the position vectors of the atomic sites k and j, respectively, after strain. Equations (1) and (2) can be related through the transformation gradient $\boldsymbol{F}$:

$$\Delta \boldsymbol{x}_{jk} \approx \boldsymbol{F} \cdot \Delta \boldsymbol{X}_{jk}. \tag{3}$$

The strain tensor is then obtained by

$$\boldsymbol{E} = \tfrac{1}{2}(\boldsymbol{F}^{\mathbf{T}}\boldsymbol{F} - \boldsymbol{I}), \tag{4}$$

where $\mathbf{I}$ is the identity tensor.
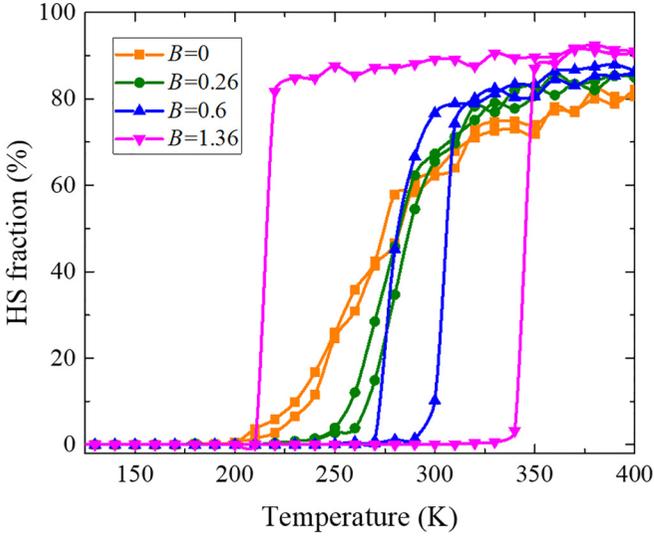
FIG. 2. Simulated spin-transition curves of the [Fe(pyrazine)][Ni(CN)$_4$] SCO compound, showing the thermal evolution of the HS fraction for different values of the parameter B, which controls the strength of the elastic interactions (lines are guides to the eye).

III. RESULTS AND DISCUSSIONS

A. Spatiotemporal aspects of the HS-to-LS relaxation process

First, the thickness of the modeled device is set to $N_{tot} = 8$ unit cells. Along the y direction, one extremity of the cantilever is fixed, while the other one is free to move. Two cases are considered: (1) the case of an all-active system ($N_I = 0$) in which all Fe sites can switch between the LS and HS states, and (2) the case of a bimorph system ($N_I = 4$) composed of four SCO active (at the top) and four inactive (HS) [Fe(pyrazine)][Ni(CN)$_4$] layers (at the bottom). As described in the Part I of our work [45], the cooperative phenomena, controlled by the height of the elastic energy barrier, are driven by the value of the parameter B in the expression of the potential connecting the SCO-active Fe sites:

$$E_{\text{cooperativity}}$$
$$= \frac{B}{2}\Big(b_0[c_0 - (R - R_{LS})]^2 + a_0(R - R_{LS})^2$$
$$- \sqrt{4J_0^2 + \{b_0[c_0 - (R - R_{LS})]^2 + a_0(R - R_{LS})^2\}^2}\Big),$$
$$(5)$$

where a_0, b_0, and c_0 are parameters that control the concavity of the double-well potential energy, R_{LS} is the lattice constant of the equilibrium LS state, and J_0 is an off-diagonal element. In the following, except otherwise mentioned, in the simulations, we set the parameter B to 0.6, which allows us to correctly reproduce the first-order spin transition curve with a 30-K-wide thermal hysteresis loop centered at ~290 K, which was experimentally observed for the bulk compound [Fe(pyrazine)][Ni(CN)$_4$] [54] (see Fig. 2). At this stage, it may be worth noting that, in ultrathin SCO films, one may expect a modification of SCO properties [32,55–58], but these finite-sized effects will be ignored in the present
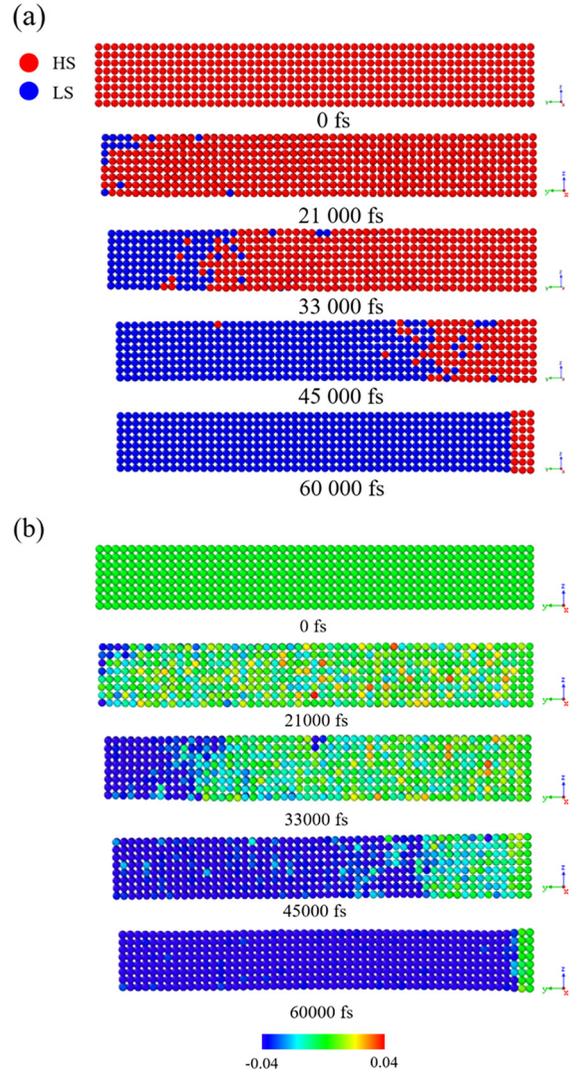

FIG. 3. Selected snapshots showing the spatial distribution of (a) the spin-state configuration and (b) the local lattice strain in the all-active system ($N_I = 0$) at different times during the high-spin (HS)-to-low-spin (LS) relaxation process at 100 K (for $B = 0.6$). In (a), the red and blue balls represent HS and LS sites, respectively. In (b), the color scale changes from red (tensile) to blue (compressive) strain through green (initial, zero strain) colors.

calculations because the change of sample geometry which plays an important role in the finite-sized effect is not considered in the present simulation.

Figure 3(a) depicts selected snapshots showing the spatial distribution of the spin-state configuration in the all-active system ($N_I = 0$), during the HS-to-LS relaxation process at 100 K. In these representations, it is worth mentioning that each unit cell of the [Fe(pyrazine)][Ni(CN)$_4$] compound is simply represented by a red (or a blue) ball, depending on whether the corresponding Fe^{2+} ion is in the HS (or LS) state. This is a usual representation employed for spring-ball models, such as electroelastic, mechanoelastic, or atom-phonon models, in which the SCO units are represented by fictitious spins or spherical objects. Nevertheless, in this paper, it is important to remember that a realistic, all-atom structure

is always considered in the simulations. In agreement with previous experimental and theoretical observations [59–63], we find that the HS-to-LS relaxation takes place via a heterogeneous phase separation process, characterized by the nucleation and the growth of a stable LS domain within the initial, metastable HS phase. In detail, the nucleation of a LS domain is found to occur at the top left corner of the system (where no mechanical constraint is applied) at ∼21 ps, followed by the propagation of a LS/HS phase boundary throughout the cantilever to reach the opposite rigid border at $t \approx 60$ ps. The nucleation of a LS domain is because the molecules at the corner of the cantilever need to overcome a lower energy barrier to switch from one spin state to another in comparison with those located at the edges or in the bulk. This phenomenon is different from the observation in Part I of our work [45] since, for this latter, periodic boundary conditions have been applied to simulate an infinite system. In this case, the transformation is homogeneous, and no HS or LS clustering is expected to be detected during the spin-state switching. By comparing the fully relaxed lattice (at $t = 60$ ps) to the initial HS lattice (at $t = 0$), we can note that the complete relaxation of the structure from the HS to the LS state is accompanied by a sizeable contraction of the unit cell, which leads to a visible decrease of the size of the system by 5% along the y direction. For the same time delays, corresponding snapshots of the local strain in the structure, calculated from the simulations, are shown in Fig. 3(b). As the lattice state at $t = 0$ (full HS state) is taken as the reference in the present simulation, positive and negative values of the local strain correspond to tensile and compressive deformations, respectively. Overall, the simulated strain maps exhibit similar features to the spin-state configuration, indicating a clear correlation between the local spin state and the local strain of the structure. Specifically, as depicted in Fig. 3(b), a compressive strain region (deep blue color) is observed at the top left corner of the beam at $t = 21$ ps, in accordance with the nucleation of the LS domain. This compressive region then grows all along the cantilever, following the evolution of the spin-state configuration displayed in Fig. 3(a). At this stage, we shall underline that the typical relaxation times observed in our investigations are of the order of a few tens of picoseconds (depending on the geometry of the system), which is significantly faster than what one would expect for an SCO system at 100 K [64]. This observation is linked to the fact that the intramolecular energy barrier was set in our model [45] to significantly lower values than the experimentally observed ones, to fit the relaxation time into the timeframe of the MD simulations. To overcome this drawback, future work may focus on using coarse-grained or accelerated MD methods [65,66].

By comparison, Fig. 4(a) depicts selected snapshots of the spatial distribution of the local spin state during the relaxation process in the case of the bimorph system ($N_I = 4$), composed of four active (top) and four inactive (bottom) [Fe(pyrazine)][Ni(CN)$_4$] layers. Again, the left extremity of the bimorph cantilever is kept free to move. We observe that a LS domain appears at the top left corner of the beam at $t \approx 32$ ps, i.e., with a delay compared with the case of the all-active system (Fig. 3). At this moment, the concentration of these

newly formed LS sites is already found to induce a slight bending of the cantilever. Later, at $t = 67$ ps, as the LS domain grows, a larger macroscopic distortion of the lattice (which results in a significant deflection of the device) is observed, and interestingly, a second LS domain is formed in the middle of the cantilever. As depicted in the local strain mapping shown in Fig. 4(b), we can rationalize this observation by the fact that the bending of the lattice generates a compressive stress within the active part, which results in a local negative strain (indicated by an arrow at $t = 32$ ps), favoring the nucleation of this second LS domain. Finally, from $t = 97$ to 232 ps, the two formed LS domains merge and grow until reaching the rigid edge of the cantilever. Interestingly, in the stationary state (at $t = 232$ ps), we observe that a few SCO sites at the interface between the active and inactive parts of the system remain blocked in the HS state, presumably because they are submitted to a permanent tensile stress coming from the lattice misfit with the inactive (HS) part of the cantilever. Indeed, as displayed in Fig. 4(b), a detailed observation of the local strain mapping in the final relaxed state (at $t = 232\,000$ fs) shows that strain gradients exist in both the active and inactive layers of the cantilever. It appears that the magnitude of compressive strain slightly decreases within the active part when approaching the interface. In the same way, the distribution of strain in the inactive part of the structure shifts from compressive to tensile deformation (from green to red color). Such a gradient of strain within the structure is an obvious consequence of the bending of the cantilever. In addition, due to the existence of the HS/LS interface (between the inactive and active layers), the mismatch between HS and LS lattices gives rise to a compressive (resp. tensile) stress in the material near the interface in the inactive (resp. active) part, indicating competing mechanical effects between the active and inactive parts of the bimorph system.

B. Relaxation curves of the molecular spin state

Figure 5(a) compares the thermal relaxation curves, displaying the time evolution of the fraction of HS sites, in the all-active system ($N_I = 0$) and in the bimorph system ($N_I = 4$). As shown in Fig. 5(a), the time needed by the system to reach the relaxed stationary state is considerably extended due to the presence of the inactive layers. Indeed, this inactive part (which remains in the HS state) produces a tensile stress in the active layers, as the latter switch from the HS to the LS state, due to the lattice misfit at the interface. As this tensile stress favors the HS state, the relaxation process is submitted to a law of moderation, resulting in a slowdown of the relaxation kinetics. Interestingly, if both ends of the bimorph are clamped, this effect is further amplified because the structure cannot relieve any more part of the tensile stress by the bending movement. Figure 5(b) depicts the evolution of the HS-to-LS relaxation kinetics in the bimorph system (with $N_{\text{tot}} = 8$) upon varying the number of inactive layers N_I from 1 to 7. Remarkably, a considerable slowdown of the relaxation kinetics can be observed when increasing the thickness of the inactive part of the cantilever. A straightforward explanation is that the increase of the thickness of the inactive (HS) part contributes to
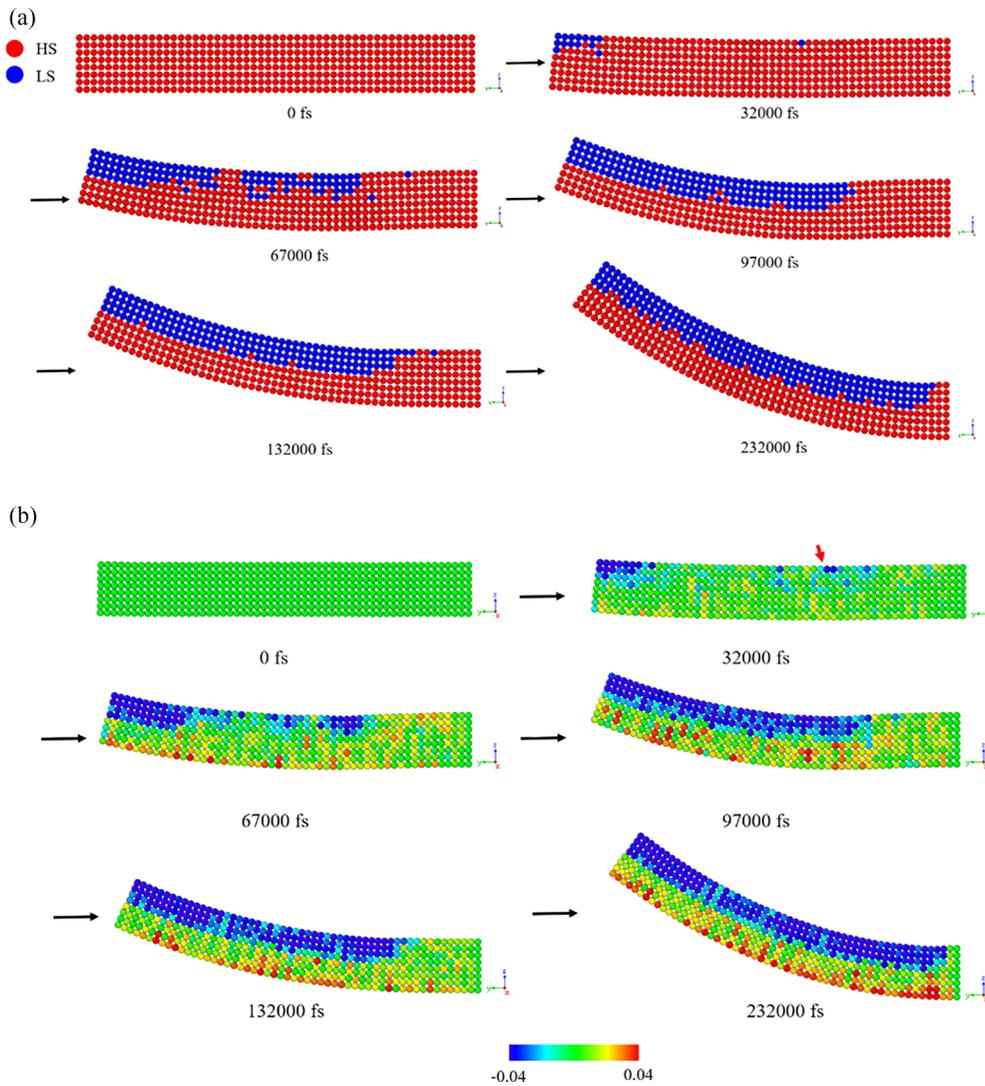
FIG. 4. Selected snapshots showing the spatial distribution of (a) the spin-state configuration and (b) the local lattice strain in the bimorph cantilever ($N_I = 4$), at different times during the high-spin (HS)-to-low-spin (LS) relaxation process at 100 K (for $B = 0.6$). In (a), the red and blue balls represent HS and LS sites, respectively. In (b), the color scale changes from red (tensile) to blue (compressive) strain through green (initial, zero strain) colors.

generating tensile stress on the active part, whereas the increased stiffness of the structure prevents the release of this stress. These effects result in a longer lifetime of the metastable HS state in the active layers. Interestingly, as shown in Fig. 5(b) (black curve), in the extreme case where $N_I = 7$ (i.e., $N_S = 1$), it appears that only ∼15% of the SCO sites in the active layers switch into the LS form in the stationary state.

Qualitatively comparable results have been obtained from the simulations of the spin-transition properties of SCO monolayers on a substrate (using spring-ball models) or from the simulations of bimorph nanoparticles in which a SCO core is surrounded by an inactive shell [32,37–39,42–44,67–70]. These different theoretical investigations have the advantage to give a description of the elastic mechanisms involved in the switching process of such hybrid nanomaterials and are in good qualitative agreement with the different accessible experimental observations.

C. Deflection behaviors

To investigate the actuating performance of the modeled bimorph system, we focus on the deflection, which is defined as the distance between the instantaneous and initial vertical positions of the free extremity of the cantilever. Figure 6(a) shows the time evolution of the deflection in the bimorph actuator ($N_{tot} = 8$) associated with the HS-to-LS relaxation process for different thicknesses of the inactive part (N_I ranging from 1 to 7 layers). For each simulated system, damped oscillations of the deflection of the cantilever are observed before reaching a stationary mechanical state, defining the equilibrium deflection. It is worth mentioning that these oscillations take place on a longer time scale (nanoseconds) than the relaxation kinetics of the molecular spin state [∼100 ps, see Fig. 5(b)], meaning that the spin-state equilibrium is reached faster than the mechanical equilibrium of the cantilever. This oscillatory movement presumably comes from the fact that the fast-switching kinetics of the molecular
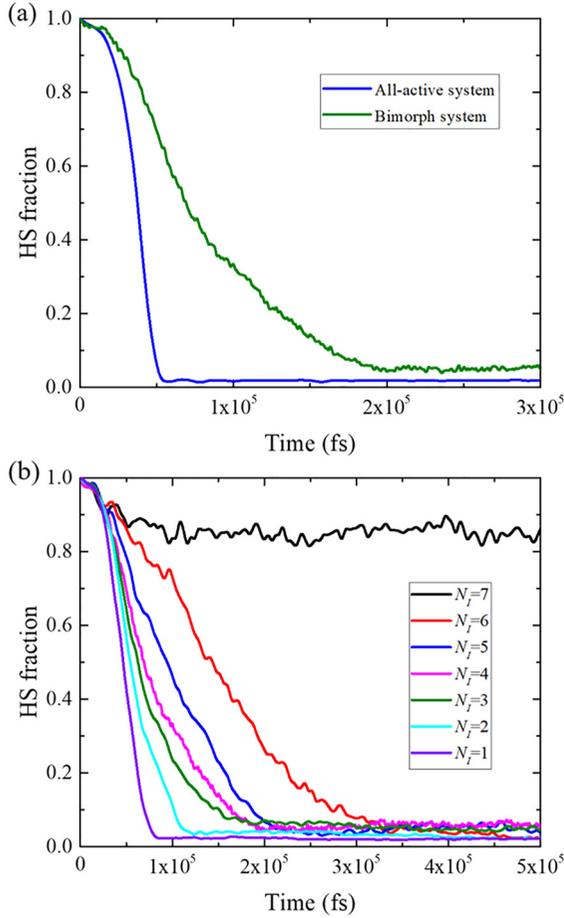
FIG. 5. (a) Time evolution of the high-spin (HS) fraction during the relaxation process at $T = 100$ K (for $B = 0.6$), in the all-active system ($N_I = 0$) and in the bimorph system ($N_I = 4$). (b) Time evolution of the HS fraction during the relaxation process in the bimorph system for different numbers N_I of inactive layers from 1 to 7.

FIG. 6. (a) Time evolution of the deflection of the bimorph cantilever ($N_{\text{tot}} = 8$) during the high-spin (HS)-to-low-spin (LS) relaxation process (at 100 K, $B = 0.6$) for different thicknesses of the inactive part N_I ranging from 1 to 7 layers. (b) Equilibrium deflection of the bimorph actuator as a function of N_I deduced from the present molecular dynamics (MD) simulations and from the Euler-Bernoulli's beam theory (lines are guides to the eye).

spin state initially produces an overshoot of the deflection of the beam, so that the system finally reaches a mechanical equilibrium state by oscillating at its natural bending frequency. It may be worth mentioning here that similar damped mechanical oscillations have been recently observed using time-resolved electron microscopy upon pulsed laser excitation of SCO nanoparticles [71]. We can thus suggest that those experimental findings might have the same origin as in the present simulations, i.e., a mismatch between the time scales of the SCO and the natural stretching frequency of the particles.

As it can be expected, the equilibrium deflection strongly depends on the number of inactive layers N_I. The black curve in Fig. 6(b) shows that the equilibrium deflection exhibits a nonmonotonous behavior as a function of N_I and passes through a maximum ($\delta \approx 100$ Å) for $N_I = 4$, i.e., when the thicknesses of the active and inactive regions are equal. Importantly, the atomistic approach used in this paper allows us to assess macroscopic/mesoscopic quantities, such as mechanical deflections, which can also be inferred from continuum mechanics models. Indeed, according to the Euler-Bernoulli
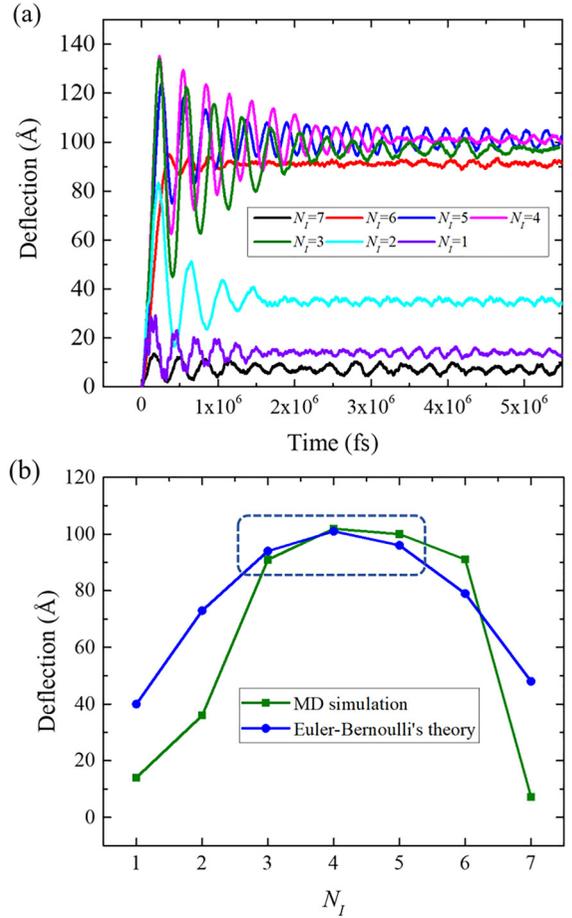
beam theory [25,72], the curvature (k) of a bimorph cantilever can be expressed as

$$k = \frac{6\left(\alpha_i \Delta T + \frac{\Delta L}{L} - \alpha_s \Delta T\right)(1 + m)^2}{h\left[3(1 + m)^2 + (1 + mn)\left(m^2 + \frac{1}{mn}\right)\right]}, \quad (6)$$

$$m = \frac{h_s}{h_i}, \quad (7)$$

$$n = \frac{E_s}{E_i}, \quad (8)$$

$$h = h_s + h_i, \quad (9)$$

where the subscripts s and i stand for the switchable and inactive parts of the bimorph system, respectively. Here, ΔT is the working temperature range, ΔL is the change of length induced by SCO, α is the coefficient of thermal expansion, E is the Young's modulus, and h is the thickness. The deflection

δ can be estimated through the following relationship:

$$\delta = \frac{kL^2}{2}, \qquad (10)$$

where L is the length of the cantilever. Here, $E_i = 10.4$ GPa and $E_s = 13.5$ GPa are taken from Ref. [73]. It should be noted that the first-order HS → LS spin transition causes a spontaneous strain, which is usually orders of magnitude larger than the strain induced by the thermal expansion. Thus, the coefficients of thermal expansion in Eq. (5) are ignored in the present calculation ($\alpha_i = a_i = 0$). By comparison with the result of our MD simulations, the deflections of the various studied systems extracted from the Euler-Bernoulli theory are also displayed in Fig. 6(b). Like our MD simulations, the deflection of the bimorph cantilever follows a bell-shaped curve as a function of N_I, reaching a maximum for $N_I = 4$. Overall, the deflection values obtained from the two approaches are in good agreement within the range $N_I = 3 - 5$. As shown in Fig. 6(b), for lower and higher values of N_I, the results from these two methods show larger deviations. Such a difference can probably arise from the fact that the effective thermomechanical properties are modified when these materials become extremely thin. Our MD simulations show that only a reduced fraction of SCO complexes can effectively switch into the LS state [particularly in the case $N_I = 7$, as shown in Fig. 5(b)], which can explain why the deflection is smaller than the one extracted from the Euler-Bernoulli theory.

We have also investigated the effect of the total thickness (N_{tot}) of the cantilever on the deflection. To this aim, a ratio of $N_I/N_S = 1$ is selected (i.e., equal thicknesses are considered for the active and inactive parts), which corresponds to the case where the bimorph system exhibits the largest deflection at the thermal and mechanical equilibrium. Bimorph cantilevers with sizes $N_{\text{tot}} = 6, 8, 10$, and 12 (i.e., $N_I = N_S = 3$, 4, 5, and 6) were analyzed and the time evolution of the deflection of these bimorphs was followed. As shown in Fig. 7(a), we observe that both the amplitude and the period of the oscillations are reduced when increasing the total thickness of the cantilever, primarily due to the increased bending stiffness of the whole structure, n.b. the increase of mass acts in the opposite way. In concomitance, we also observe that the equilibrium deflection is significantly reduced with the increase of the total thickness. Indeed, as depicted in Fig. 7(b), the deflection at the equilibrium state drops from 134 to 72 Å upon increasing the total thickness of the cantilever from 6 to 12 [Fe(pyrazine)][Ni(CN)$_4$] layers. It is worth saying that, in this case ($N_I/N_S = 1$), the main parameter impacting the equilibrium deflection of thin actuators is the length to thickness ratio. Additionally, as shown in Fig. 7(b), the equilibrium deflections extracted from the present MD simulations are found to be in good agreement with the values calculated using the Euler-Bernoulli theory, which further validates our approach.

D. Effect of the cooperativity

The influence of the cooperativity of the SCO material on the HS-to-LS relaxation process and the actuating performance of the cantilever are investigated by varying the value of the parameter B, which drives the strength of the
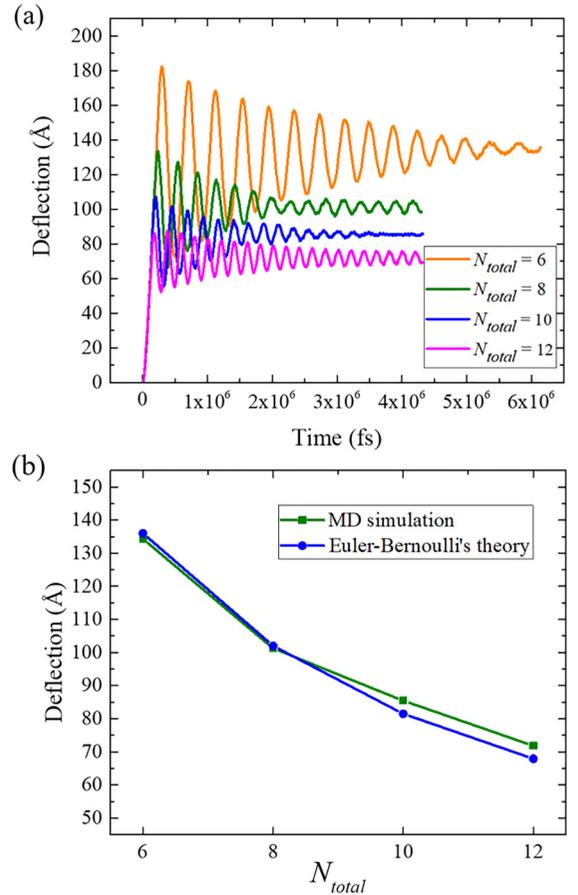

FIG. 7. (a) Time dependence of the deflection of the bimorph cantilever for different thicknesses during the high-spin (HS)-to-low-spin (LS) relaxation process ($T = 100$ K, $B = 0.6$). (b) Equilibrium deflection of the bimorph cantilever for different thicknesses inferred from the present molecular dynamics (MD) simulations and from the Euler-Bernoulli's beam theory (lines are guides to the eye).

elastic interactions. To this aim, three additional values of B ($B = 0, 0.26$, and 1.36) were investigated, which correspond, respectively, to the case of a gradual spin conversion (with no hysteresis loop), a transition with a narrow ($\sim$5-K-wide) hysteresis loop, and a transition with a large ($\sim$130-K-wide) thermal hysteresis loop, as depicted in Fig. 2.

Figures 8(a) and 8(b) show the time evolution of the HS fraction in the all-active system ($N_I = 0$) for different values of B. As B decreases, the shape of the relaxation curves switches from sigmoidal to exponential (or stretched exponential), which indicates a change from a strongly cooperative behavior to a weakly cooperative behavior [74–77]. This lengthening of the lifetime of the metastable HS state in the highly cooperative case occurs because the strong elastic interactions produce a high energy barrier that needs to be overcome to relax into the LS state. Interestingly, clear damped oscillations are observed in the time evolution of both the HS fraction and of the length of the cantilever, as shown in Fig. 8(c). The damped oscillation periods of the spin state are close to those of the length of the cantilever for each value of B. Moreover, the amplitude and the period of these oscillations appear to be strongly dependent on the
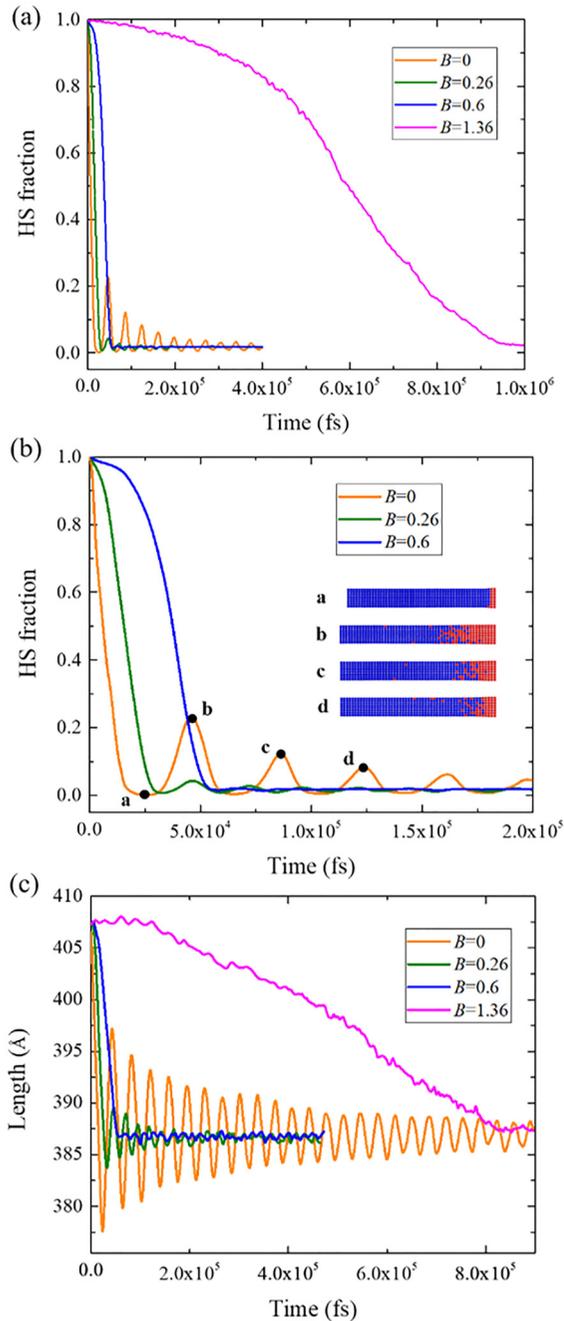
FIG. 8. (a) Time evolution of the high-spin (HS) fraction during the HS-to-low-spin (LS) relaxation process at $T = 100$ K in the all-active system ($N_I = 0$) for various values of B. (b) Zoom showing the time evolution of the HS fraction at short timescales for $B = 0$, 0.26, and 0.6. Inset: Snapshots of the spatial distribution of the spin-state configuration at different times (marked by black dots) in the case $B = 0$. The red and blue balls represent HS and LS sites, respectively. (c) Time evolution of the length of the all-active system ($N_I = 0$) during the HS-to-LS relaxation process at $T = 100$ K for various values of B.

cooperative character of the SCO material. Indeed, for low cooperativity ($B = 0$), it appears that the spin-state relaxation time is much faster than the period of stretching oscillations of the cantilever ($T_{\text{stretching}} \approx 36$ ps), which generates an initial

overshoot in the longitudinal deformation of the cantilever. The latter thus releases the excess mechanical energy by oscillating at the natural stretching frequency of the structure. This oscillation frequency is found to depend on the strength of the elastic interactions B. Indeed, we observe that the oscillation frequency becomes larger when increasing B, which parallels the increasing stiffness of the SCO material. The damped oscillations observed in the temporal evolution of the HS fraction show that the molecular spin state is linked to the global deformation (strain) of the structure, i.e., the oscillation of the beam provokes an oscillation of the HS fraction. However, the amplitude of the oscillations (in terms of both HS fraction and length of the cantilever) are found to be reduced with B because the switching kinetics between the LS and HS states becomes slow in comparison with the natural stretching frequency of the cantilever. As an example, for $B = 1.36$, the full relaxation into the LS state is completed in $\sim$1 ns, which is significantly longer than the period of stretching oscillations $T_{\text{stretching}}$ of the structure, so that no oscillations are observed at all in this case.

Following this study of the all-active, unimorph cantilever, we have also investigated the effect of cooperativity on the time evolution of the HS fraction and the deflection of the bimorph cantilever. To this aim, we have studied the case $N_I = N_S = 4$, which enables the largest deflection to occur, as discussed previously. The time evolution of the deflection δ of the cantilever during the HS-to-LS relaxation process is plotted in Fig. 9(a) for different values of B. The first observation is that an identical deflection ($\delta \approx 100$ Å) is obtained at the equilibrium state, independently of the value of B. Indeed, since the value of B is tuned for both the inactive and the switchable layers of the cantilever, the ratio of the Young's moduli of the two parts (E_s/E_i) remains constant, which implies no change of the equilibrium deflection [see Eq. (5)]. However, large damped oscillations of the deflection are observed before reaching the stationary state. These oscillations to reach the mechanical equilibrium state take place at the natural bending frequency of the cantilever. Interestingly, as the cooperativity (B) is reduced, both the amplitude and the period of the oscillations are increased [see Fig. 9(b)]. This comes from the fact that the reduction of B implies a softening of the lattice, which becomes more deformable, thus allowing larger deflections to occur. In addition, as both the oscillation frequency and the damping rate are proportional to $\sqrt{E}$, we observe that the reduction of B also leads to an increase of the bending oscillation period of the bimorph system, going from $\sim$300 ps ($\sim$3.33 GHz) to $\sim$400 ps ($\sim$2.50 GHz) and a concomitant decrease of the damping rate when the value of B is decreased from 0.6 to 0 [Fig. 9(b)]. By comparison, the time evolution of the HS fraction for the different values of B is shown in Fig. 10(a). As already mentioned, the switching kinetics between the LS and HS states is considerably slowed down for large values of B. In the case $B = 0$, the HS fraction is found to oscillate with two characteristic periods, $T_{\text{stretching}} = 36$ ps and $T_{\text{bending}} = 400$ ps, which respectively correspond to the natural stretching period (as it was shown through the study of the all-active system) and the natural bending period of the cantilever. Thus, we find that the time evolution of the HS fraction faithfully follows the deformations of the studied bimorph system, clearly showing
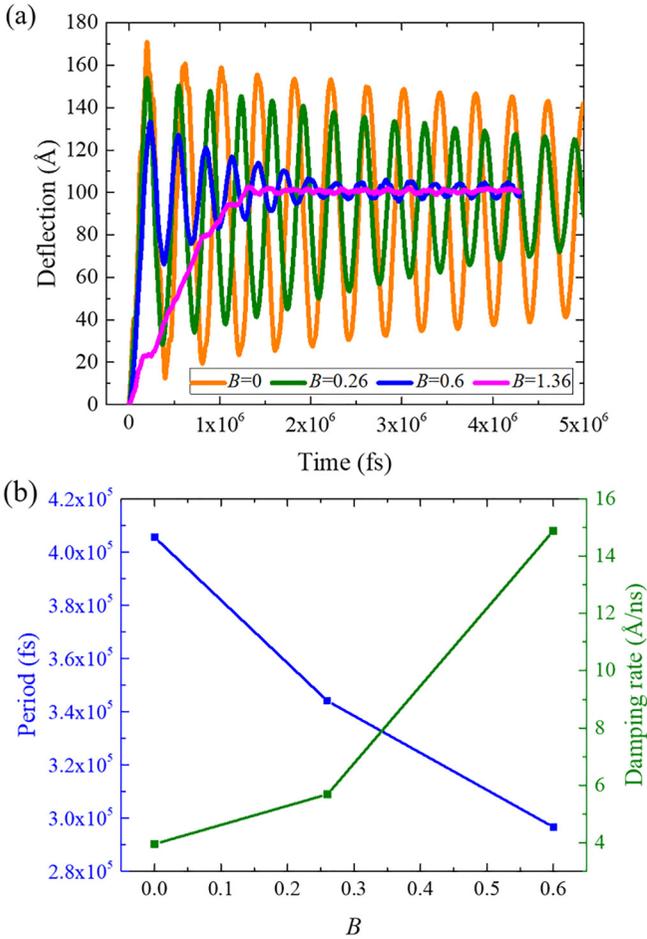
FIG. 9. (a) Time evolution of the deflection of the bimorph cantilever (in the case $N_I = N_S = 4$) during the high-spin (HS)-to-low-spin (LS) relaxation process at $T = 100$ K for various values of B. (b) Evolution of the period and damping rate of the deflection oscillations as a function of B.

the interplay between the molecular electronic state and the local stress/strain within the structure. When B is increased, the amplitude of the oscillations of the HS fraction is largely reduced (for $B = 0.26$ and 0.6, only the bending oscillations of the cantilever have a visible effect on the HS fraction). Again, this effect arises from the fact that an increase of cooperativity has the effect of progressively slowing down the HS $\leftrightarrow$ LS switching kinetics, so that the HS fraction will be first decoupled from the fast-stretching oscillations and, in a second time, from the slower bending oscillations of the cantilever. (Note that a slow relaxation kinetics also has the effect of preventing an overshoot effect in the bending or in the longitudinal shrinkage of the cantilever, which could lead to large oscillations.) Finally, as shown in Figs. 9(a) and 10(a), in the case of a highly cooperative SCO material ($B = 1.36$), the full LS state and the equilibrium deflection are reached within ~1.4 ns with no oscillations.

IV. CONCLUSIONS

In conclusion, we have performed a theoretical study to investigate the spin-state relaxation process and the re-

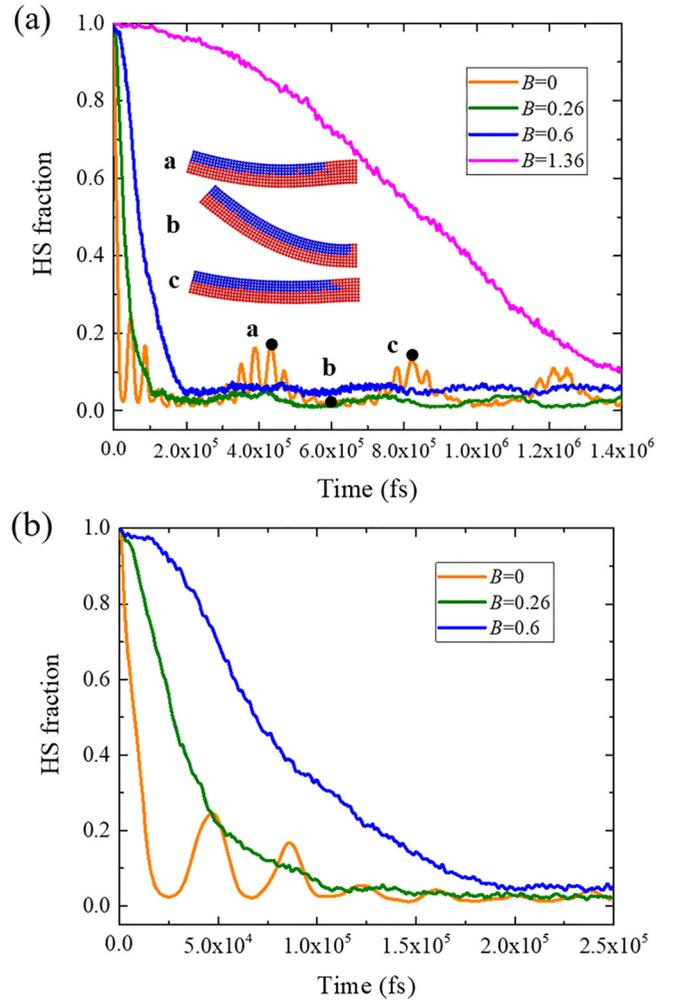
FIG. 10. (a) Time evolution of the high-spin (HS) fraction in the bimorph cantilever (in the case $N_I = N_S = 4$) during the HS-to-low-spin (LS) relaxation process at $T = 100$ K for various values of B. Inset: Snapshots of the spatial distribution of the spin-state configuration at different times (marked by black dots) in the case $B = 0$. The red and blue balls represent HS and LS sites, respectively. (b) Zoom showing the time evolution of the HS fraction at short timescales for $B = 0$, 0.26, and 0.6.

sulting deformation of a bimorph cantilever beam of the [Fe(pyrazine)][Ni(CN)$_4$] SCO material, through all-atom MD simulation based on our recently constructed FF. Spatiotemporal aspects of the spin transition were investigated by visualizing the real-time spin-state configuration and the local strain on each SCO site during the HS-to-LS relaxation process. Interestingly, the phase separation process and its dynamics appear to be significantly influenced by the presence of the inactive layers of the actuator, which exert tensile stress on the active layers, while the concomitant bending of the cantilever induces the formation of additional LS domains during the nucleation and growth process. Importantly, the deflection obtained from our simulations at equilibrium is found to be in good agreement with that from the Euler-Bernoulli continuum mechanics model, particularly for sufficiently thick systems. Interestingly, in some cases, clear stretching and bending damped oscillations of the cantilever (at the natural

frequencies of the structure) are observed during the switching process before reaching a mechanical equilibrium state. The amplitude and frequency of these oscillations are found to depend on the total thickness of the cantilever and on the cooperativity (stiffness) of the SCO material. Oscillations with particularly large amplitudes are observed in the case of fast spin-state switching (observed for weakly cooperative materials) presumably due to an initial overshoot in the deformation of the structure. Remarkably, damped oscillations were also observed in the time evolution of the HS fraction during the relaxation process, showing the intimate interplay between the deformation state of the cantilever and the spin state of the molecules.

[1] H. Ma, X. Xiao, X. Zhang, and K. Liu, Recent advances for phase-transition materials for actuators, J. Appl. Phys. **128**, 101101 (2020).

[2] J. D. Madden, Mobile robots: Motor challenges and materials solutions, Science **318**, 1094 (2007).

[3] S. Kim, C. Laschi, and B. Trimmer, Soft robotics: A bioinspired evolution in robotics, Trends Biotechnol. **31**, 287 (2013).

[4] W. Huang, Z. Ding, C. Wang, J. Wei, Y. Zhao, and H. Purnawali, Shape memory materials, Mater. Today **13**, 54 (2010).

[5] B. T. Lester, T. Baxevanis, Y. Chemisky, and D. C. Lagoudas, Review and perspectives: Shape memory alloy composite systems, Acta Mech. **226**, 3907 (2015).

[6] J. Cao, W. Fan, Q. Zhou, E. Sheu, A. Liu, C. Barrett, and J. Wu, Colossal thermal-mechanical actuation via phase transition in single-crystal microcantilevers, J. Appl. Phys. **108**, 083538 (2010).

[7] A. Rúa, F. E. Fernández, and N. Sepúlveda, Bending in VO2-coated microcantilevers suitable for thermally activated actuators, J. Appl. Phys. **107**, 074506 (2010).

[8] K. Liu, C. Cheng, Z. Cheng, K. Wang, R. Ramesh, and J. Wu, Giant-amplitude, high-work density microactuators with phase transition activated nanolayer bimorphs, Nano Lett. **12**, 6302 (2012).

[9] P. Gütlich, A. Hauser, and H. Spiering, Thermal and optical switching of iron(II) complexes, Angew. Chem. Int. Ed. **33**, 2024 (1994).

[10] M. A. Halcrow, *Spin-Crossover Materials: Properties and Applications* (John Wiley & Sons, Chichester, 2013).

[11] G. Molnár, S. Rat, L. Salmon, W. Nicolazzi, and A. Bousseksou, Spin crossover nanomaterials: From fundamental concepts to devices, Adv. Mater. **30**, 1703862 (2018).

[12] A. Bousseksou and G. Molnár, The spin-crossover phenomenon: Towards molecular memories, C. R. Chim. **6**, 1175 (2003).

[13] P. Guionneau, Crystallography and spin-crossover. A view of breathing materials, Dalton Trans. **43**, 382 (2014).

[14] E. Collet and P. Guionneau, Structural analysis of spin-crossover materials: From molecules to materials [Études structurales des matériaux à conversion de spin: De la molécule aux matériaux], C. R. Chim. **21**, 1133 (2018).

[15] S. Pillet, Spin-crossover materials: Getting the most from x-ray crystallography, J. Appl. Phys. **129**, 181101 (2021).

[16] M. Grzywa, R. Röß-Ohlenroth, C. Muschielok, H. Oberhofer, A. Błachowski, J. Żukrowski, D. Vieweg, H.-A. K. Von Nidda, and D. Volkmer, Cooperative large-hysteresis spin-crossover transition in the iron(II) triazolate [Fe(ta)$_2$] metal-organic framework, Inorg. Chem. **59**, 10501 (2020).

[17] M. D. Manrique-Juárez, S. Rat, L. Salmon, G. Molnár, C. M. Quintero, L. Nicu, H. J. Shepherd, and A. Bousseksou, Switchable molecule-based materials for micro- and nanoscale actuating applications: Achievements and prospects, Coord. Chem. Rev. **308**, 395 (2016).

[18] H. J. Shepherd, I. A. Guralskiy, C. M. Quintero, S. Tricard, L. Salmon, G. Molnár, and A. Bousseksou, Molecular actuators driven by cooperative spin-state switching, Nat. Commun. **4**, 2607 (2013).

[19] I. A. Guralskiy, C. M. Quintero, J. S. Costa, P. Demont, G. Molnár, L. Salmon, H. J. Shepherd, and A. Bousseksou, Spin crossover composite materials for electrothermomechanical actuators, J. Mater. Chem. C **2**, 2949 (2014).

[20] M. D. Manrique-Juárez, F. Mathieu, A. Laborde, S. Rat, V. Shalabaeva, P. Demont, O. Thomas, L. Salmon, T. Leichle, L. Nicu *et al.*, Micromachining-compatible, facile fabrication of polymer nanocomposite spin crossover actuators, Adv. Funct. Mater. **28**, 1801970 (2018).

[21] M. Piedrahita-Bello, B. Martin, L. Salmon, G. Molnár, P. Demont, and A. Bousseksou, Mechano-electric coupling in P(VDF–TrFE)/spin crossover composites, J. Mater. Chem. C **8**, 6042 (2020).

[22] M. Piedrahita-Bello, J. E. Angulo-Cervera, A. Enriquez-Cabrera, G. Molnár, B. Tondu, L. Salmon, and A. Bousseksou, Colossal expansion and fast motion in spin-crossover@polymer actuators, Mater. Horiz. **8**, 3055 (2021).

[23] M. Piedrahita-Bello, Y. Zan, A. Enriquez-Cabrera, G. Molnár, B. Tondu, L. Salmon, and A. Bousseksou, Effect of the spin crossover filler concentration on the performance of composite bilayer actuators, Chem. Phys. Lett. **793**, 139438 (2022).

[24] M. Piedrahita-Bello, X. Yang, S. E. Alavi, G. Molnár, L. Salmon, and A. Bousseksou, Anisotropic spin-crossover composite actuators displaying pre-programmed movements, Sens. Actuators B: Chem. **393**, 134147 (2023).

[25] Y. Zan, M. Piedrahita-Bello, S. E. Alavi, G. Molnár, B. Tondu, L. Salmon, and A. Bousseksou, Soft actuators based on spin-crossover particles embedded in thermoplastic polyurethane, Adv. Intell. Syst. **5**, 2200432 (2023).

[26] M. D. Manrique-Juárez, S. Rat, F. Mathieu, D. Saya, I. Séguy, T. Leïchlé, L. Nicu, L. Salmon, G. Molnár, and A. Bousseksou, Microelectromechanical systems integrating molecular spin crossover actuators, Appl. Phys. Lett. **109**, 061903 (2016).

[27] M. D. Manrique-Juárez, F. Mathieu, V. Shalabaeva, J. Cacheux, S. Rat, L. Nicu, T. Leïchlé, L. Salmon, G. Molnár, and A. Bousseksou, A bistable microelectromechanical system actuated by spin-crossover molecules, Angew. Chem. Int. Ed. **129**, 8186 (2017).

[28] M. Urdampilleta, C. Ayela, P.-H. Ducrot, D. Rosario-Amorin, A. Mondal, M. Rouzières, P. Dechambenoit, C. Mathonière, F. Mathieu, I. Dufour *et al.*, Molecule-based microelectromechanical sensors, Sci. Rep. **8**, 8016 (2018).

[29] J. Dugay, M. Giménez-Marqués, W. J. Venstra, R. Torres-Cavanillas, U. N. Sheombarsing, N. Manca, E. Coronado, and H. S. Van Der Zant, Sensing of the molecular spin in spin-crossover nanoparticles with micromechanical resonators, J. Phys. Chem. C **123**, 6778 (2019).

[30] J. E. Angulo-Cervera, M. Piedrahita-Bello, F. Mathieu, T. Leichle, L. Nicu, L. Salmon, G. Molnár, and A. Bousseksou, Investigation of the effect of spin crossover on the static and dynamic properties of MEMS microcantilevers coated with nanocomposite films of [Fe(Htrz)$_2$(trz)](BF$_4$)@P(VDF-TrFE), Magnetochemistry **7**, 114 (2021).

[31] M. Paez-Espejo, M. Sy, and K. Boukheddaden, Unprecedented bistability in spin-crossover solids based on the retroaction of the high spin low-spin interface with the crystal bending, J. Am. Chem. Soc. **140**, 11954 (2018).

[32] M. Kelai, V. Repain, A. Tauzin, W. Li, Y. Girard, J. Lagoute, S. Rousset, E. Otero, P. Sainctavit, M.-A. Arrio *et al.*, Thermal bistability of an ultrathin film of iron(II) spin-crossover molecules directly adsorbed on a metal surface, J. Phys. Chem. Lett. **12**, 6152 (2021).

[33] A. Railean, M. Kelai, A. Bellec, V. Repain, M.-L. Boillot, T. Mallah, L. Stoleriu, and C. Enachescu, Mechanoelastic simulations of monolayer lattices of spin crossover molecules on a substrate, Phys. Rev. B **107**, 014304 (2023).

[34] Y. Singh, K. Affes, N.-I. Belmouri, and K. Boukheddaden, Clamping of spin-crossover solid inducing crystal bending and spatial spin organization, Mater. Today Phys. **27**, 100842 (2022).

[35] K. Boukheddaden and A. Bailly-Reyre, Towards the elastic properties of 3D spin-crossover thin films: Evidence of buckling effects, Europhys. Lett. **103**, 26005 (2013).

[36] K. Affes, A. Slimani, A. Maalej, and K. Boukheddaden, Electro-elastic modeling of thermal and mechanical properties of a spin crossover core/shell nanoparticle, Chem. Phys. Lett. **718**, 46 (2019).

[37] K. Affes, A. Slimani, Y. Singh, A. Maalej, and K. Boukheddaden, Magneto-elastic properties of a spin crossover membrane deposited on a deformable substrate, J. Phys.: Condens. Matter **32**, 255402 (2020).

[38] Y. Tong, M. Kelaï, K. Bairagi, V. Repain, J. Lagoute, Y. Girard, S. Rousset, M.-L. Boillot, T. Mallah, C. Enachescu, and A. Bellec, Voltage-induced bistability of single spin-crossover molecules in a two-dimensional monolayer, J. Phys. Chem. Lett. **12**, 11029 (2021).

[39] Y. Singh, H. Oubouchou, M. Nishino, S. Miyashita, and K. Boukheddaden, Elastic-frustration-driven unusual magneto-elastic properties in a switchable core-shell spin-crossover nanostructure, Phys. Rev. B **101**, 054105 (2020).

[40] H. Oubouchou, A. Slimani, and K. Boukheddaden, Elastic-frustration-driven unusual magnetoelastic properties in a

[41] A. Atitoaie, R. Tanasa, and C. Enachescu, Size dependent thermal hysteresis in spin crossover nanoparticles reflected within a Monte Carlo based Ising-like model, J. Magn. Magn. Mater. **324**, 1596 (2012).

[42] L. Stoleriu, P. Chakraborty, A. Hauser, A. Stancu, and C. Enachescu, Thermal hysteresis in spin-crossover compounds studied within the mechanoelastic model and its potential application to nanoparticles, Phys. Rev. B **84**, 134102 (2011).

[43] G. Félix, M. Mikolasek, G. Molnár, W. Nicolazzi, and A. Bousseksou, Tuning the spin crossover in nano-objects: From hollow to core-shell particles, Chem. Phys. Lett. **607**, 10 (2014).

[44] G. Félix, M. Mikolasek, G. Molnár, W. Nicolazzi, and A. Bousseksou, Control of the phase stability in spin-crossover core-shell nanoparticles through the elastic interface energy, Eur. J. Inorg. Chem. **2018**, 435 (2018).

[45] S. Mi, G. Molnár, K. Ridier, W. Nicolazzi, and A. Bousseksou, preceding paper, All-atom molecular dynamics simulation of the [Fe(pyrazine)][Ni(CN)$_4$] spin-crossover complex. I. Thermally induced spin transition in the bulk material, Phys. Rev. B **109**, 054103 (2024).

[46] S. Plimpton, Fast parallel algorithms for short-range molecular dynamics, J. Comput. Phys. **117**, 1 (1995).

[47] S. Nosé, A unified formulation of the constant temperature molecular dynamics methods, J. Chem. Phys. **81**, 511 (1984).

[48] W. G. Hoover, Canonical dynamics: Equilibrium phase-space distributions, Phys. Rev. A **31**, 1695 (1985).

[49] C. Rycroft, Voro++: A three-dimensional Voronoi cell library in C++ (Lawrence Berkeley National Lab, Berkeley, 2009).

[50] A. Stukowski, Visualization and analysis of atomistic simulation data with OVITO—The open visualization tool, Model. Simul. Mater. Sci. Eng. **18**, 015012 (2009).

[51] F. Shimizu, S. Ogata, and J. Li, Theory of shear banding in metallic glasses and molecular dynamics calculations, Mater. Trans. **48**, 2923 (2007).

[52] P. Gullett, M. Horstemeyer, M. Baskes, and H. Fang, A deformation gradient tensor and strain tensors for atomistic simulations, Model. Simul. Mater. Sci. Eng. **16**, 015001 (2007).

[53] W. Nicolazzi and S. Pillet, Structural aspects of the relaxation process in spin crossover solids: Phase separation, mapping of lattice strain, and domain wall structure, Phys. Rev. B **85**, 094101 (2012).

[54] V. Niel, J. M. Martinez-Agudo, M. C. Muñoz, A. B. Gaspar, and J. A. Real, Cooperative spin crossover behavior in cyanide-bridged Fe(II)−M(II) bimetallic 3D Hofmann-like networks (M = Ni, Pd, and Pt), Inorg. Chem. **40**, 3838 (2001).

[55] V. Shalabaeva, M. Mikolasek, M. D. Manrique-Juárez, A.-C. Bas, S. Rat, L. Salmon, W. Nicolazzi, G. Molnár, and A. Bousseksou, Unprecedented size effect on the phase stability of molecular thin films displaying a spin transition, J. Phys. Chem. C **121**, 25617 (2017).

[56] M. Kelai, A. Tauzin, A. Railean, V. Repain, J. Lagoute, Y. Girard, S. Rousset, E. Otero, T. Mallah, M.-L. Boillot *et al.*, Interface versus bulk light-induced switching in spin-crossover molecular ultrathin films adsorbed on a metallic surface, J. Phys. Chem. Lett. **14**, 1949 (2023).

[57] S. Sakaida, K. Otsubo, M. Maesato, and H. Kitagawa, Crystal size effect on the spin-crossover behavior of

{Fe(py)$_2$[Pt(CN)$_4$]} (py=pyridine) monitored by Raman spectroscopy, Inorg. Chem. **59**, 16819 (2020).

[58] T. Haraguchi, K. Otsubo, O. Sakata, A. Fujiwara, and H. Kitagawa, Strain-controlled spin transition in heterostructured metal-organic framework thin film, J. Am. Chem. Soc. **143**, 16128 (2021).

[59] N. Di Scala, N. E. I. Belmouri, M. A. P. Espejo, and K. Boukheddaden, Three-dimensional electroelastic modeling of the nucleation and propagation of the spin domains in spin-crossover materials, Phys. Rev. B **106**, 014422 (2022).

[60] M. Nishino, C. Enachescu, S. Miyashita, K. Boukheddaden, and F. Varret, Intrinsic effects of the boundary condition on switching processes in effective long-range interactions originating from local structural change, Phys. Rev. B **82**, 020409(R) (2010).

[61] R. Traiche, M. Sy, H. Oubouchou, G. Bouchez, F. o. Varret, and K. Boukheddaden, Spatiotemporal observation and modeling of remarkable temperature scan rate effects on the thermal hysteresis in a spin-crossover single crystal, J. Phys. Chem. C **121**, 11700 (2017).

[62] K. Ridier, G. Molnár, L. Salmon, W. Nicolazzi, and A. Bousseksou, Hysteresis, nucleation and growth phenomena in spin-crossover solids, Solid State Sci. **74**, A1 (2017).

[63] A. Slimani, K. Boukheddaden, F. Varret, H. Oubouchou, M. Nishino, and S. Miyashita, Microscopic spin-distortion model for switchable molecular solids: Spatiotemporal study of the deformation field and local stress at the thermal spin transition, Phys. Rev. B **87**, 014111 (2013).

[64] A. Hauser, C. Enachescu, M. L. Daku, A. Vargas, and N. Amstutz, Low-temperature lifetimes of metastable high-spin states in spin-crossover and in low-spin iron(II) compounds: The rule and exceptions to the rule, Coord. Chem. Rev. **250**, 1642 (2006).

[65] D. Hamelberg, J. Mongan, and J. A. McCammon, Accelerated molecular dynamics: A promising and efficient simulation method for biomolecules, J. Chem. Phys. **120**, 11919 (2004).

[66] S. Takada, Coarse-grained molecular simulations of large biomolecules, Curr. Opin. Struct. Biol. **22**, 130 (2012).

[67] C. Enachescu, R. Tanasa, A. Stancu, A. Tissot, J. Laisney, and M.-L. Boillot, Matrix-assisted relaxation in Fe(phen)$_2$(NCS)$_2$ spin-crossover microparticles, experimental and theoretical investigations, Appl. Phys. Lett. **109**, 031908 (2016).

[68] C. Fourmental, S. Mondal, R. Banerjee, A. Bellec, Y. Garreau, A. Coati, C. Chacon, Y. Girard, J. Lagoute, S. Rousset *et al.*, Importance of epitaxial strain at a spin-crossover molecule-metal interface, J. Phys. Chem. Lett. **10**, 4103 (2019).

[69] A. Slimani, H. Khemakhem, and K. Boukheddaden, Structural synergy in a core-shell spin crossover nanoparticle investigated by an electroelastic model, Phys. Rev. B **95**, 174104 (2017).

[70] A. Muraoka, K. Boukheddaden, J. Linares, and F. Varret, Two-dimensional Ising-like model with specific edge effects for spin-crossover nanoparticles: A Monte Carlo study, Phys. Rev. B **84**, 054119 (2011).

[71] Y. Hu, M. Picher, M. Palluel, N. Daro, E. Freysz, L. Stoleriu, C. Enachescu, G. Chastanet, and F. Banhart, Laser-driven transient phase oscillations in individual spin crossover particles, Small **19**, 2303701 (2023).

[72] S. Timoshenko, Analysis of Bi-metal thermostats, J. Opt. Soc. Am. **11**, 233 (1925).

[73] G. Félix, M. Mikolasek, H. Peng, W. Nicolazzi, G. Molnár, A. I. Chumakov, L. Salmon, and A. Bousseksou, Lattice dynamics in spin crossover nanoparticles through nuclear inelastic scattering, Phys. Rev. B **91**, 024422 (2015).

[74] K. Boukheddaden, J. Linares, H. Spiering, and F. Varret, One-dimensional Ising-like systems: An analytical investigation of the static and dynamic properties, applied to spin-crossover relaxation, Eur. Phys. J. B **15**, 317 (2000).

[75] I. Shteto, K. Boukheddaden, and F. Varret, Metastable states of an Ising-like thermally bistable system, Phys. Rev. E **60**, 5139 (1999).

[76] K. Boukheddaden, I. Shteto, B. Hôo, and F. Varret, Dynamical model for spin-crossover solids. I. Relaxation effects in the mean-field approach, Phys. Rev. B **62**, 14796 (2000).

[77] C. Enachescu, L. Stoleriu, A. Stancu, and A. Hauser, Model for elastic relaxation phenomena in finite 2D hexagonal molecular lattices, Phys. Rev. Lett. **102**, 257204 (2009).